Highly Selective Photosynthesis of Formic Acid by Unifying the Products of CO_2 Reduction and Methanol Oxidation

Zhao-Lei Liu, Meng-Ran Zhang, Guang-Xing Dong, Min Zhang, and Tong-Bu Lu*

Photocatalytic conversion of CO_2 to added-value fuels or chemicals is a promising technology for the effective utilization of the disturbing greenhouse gas, but its economic benefit is limited either by low efficiency due to the difficulty of water oxidation or by the employment of expensive sacrificial reagents. To overcome this dilemma, herein, an effective strategy is reported for the resourceful utilization of CO_2 by creating an eco-friendly bifunctional photocatalyst to achieve CO_2 photoreduction concurrent with methanol photooxidation to the uniform product of formic acid for the first time. The bifunctional photocatalyst is elaborately constructed by in situ encapsulating lead-free double perovskite ($Cs_2AgBiBr_6$, abbreviated as CABB) nanocrystals into the pores of Fe-based metal–organic framework (MIL-101(Fe)). The tight contact between CABB and MIL-101(Fe) in the resultant CABB/MIL-101(Fe) composite facilitates the efficient spatial separation of photogenerated carriers, which leads to the division of reduction and oxidation functional units. CABB/MIL-101(Fe) composites can unify the redox products into formic acid, reaching an impressive formation yield of 1375 μmol g^{-1} h^{-1} with a high selectivity of 97.8%. This work provides a viable strategy for the efficient photosynthesis of formic acid, promoting the cost-effective utilization of CO_2.

1. Introduction

The climate and environmental problems caused by ever-increasing CO_2 emission have drawn the focus of the international community,[1] and therefore, seeking feasible solutions to achieve carbon neutrality has become a common global goal.[2] Photocatalytic CO_2 reduction is a fascinating approach to realize CO_2 resource utilization,[3] which could accomplish the conversion of CO_2 to high value-added fuels or chemicals, by merely using clean and resource-abundant solar energy.[4] Among the various developed CO_2 photoreduction reaction systems, it is considered as a desirable green process to combine CO_2 reduction with water oxidation by mimicking the plant photosynthesis process.[5–15] Nevertheless, the economic benefit of this pathway is currently limited by the low efficiency due to the sluggish kinetics of water oxidation half-reaction.[16,17] To circumvent this obstacle, sacrificial agents (e.g., triethanolamine, isopropanol, and sulfite, etc.) were generally substituted for water as electron donors to rapidly annihilate photogenerated holes to facilitate the efficient utilization of photogenerated electrons in CO_2 reduction.[18–24] However, this strategy not only wastes the energy of photogenerated holes, but the employment of high-cost sacrificial agents also significantly reduces the economic efficiency of the system.[25]

To get rid of this dilemma, coupling CO_2 photoreduction and organic synthesis, that is, harnessing photogenerated holes to trigger valuable organic reactions, offers a win-win strategy for ameliorating the economic efficiency of photocatalytic CO_2 reduction.[26] In this regard, some typical organic reactions, such as dehydrogenation of hydrocarbons,[27,28] oxidation of alcohols[29,30] or amines,[31,32] transformation of unsaturated C—C bonds,[33,34] have been successfully coupled with CO_2 reduction, which avoids the employment of sacrificial agents and enable efficient utilization of photogenerated holes, thus enhancing photocatalytic efficiency of CO_2 reduction at low cost. However, current coupled systems still face the problem of poor selectivity of target products,[35,36] especially when the CO_2 reduction products are also liquid organics, and the separation of redox products will be a great challenge. Therefore, it is highly anticipated to dexterously design photocatalysts to control the selectivity of redox products. Controlling CO_2 reduction and organic oxidation to produce the same compound should be a desirable solution.

Here, we have elaborately designed a bifunctional photocatalyst through the intermarriage of metal–organic frameworks (MOFs) and perovskite materials, aiming at the efficient photoreduction of CO_2 and oxidation of CH_3OH to generate formic

Z.-L. Liu, M.-R. Zhang, G.-X. Dong, M. Zhang, T.-B. Lu
MOE International Joint Laboratory of Materials Microstructure
Institute for New Energy Materials and Low Carbon Technologies
School of Materials Science and Engineering
Tianjin University of Technology
Tianjin 300384, China
E-mail: zm2016@email.tjut.edu.cn

M. Zhang
Tianjin Key Laboratory of Organic Solar Cells and Photochemical Conversion
School of Chemistry and Chemical Engineering
Tianjin University of Technology
Tianjin 300384, China

The ORCID identification number(s) for the author(s) of this article can be found under https://doi.org/10.1002/solr.202300300.

DOI: 10.1002/solr.202300300

acid (HCOOH) as the uniform product. Of note, MOFs have been widely proven to be one of the promising photocatalysts for CO_2 conversion, owing to their unique properties such as adjustable light-harvesting ability, large surface areas, and excellent CO_2 uptake capacity.[37] In addition, the high porosity of MOFs provides internal conditions for the confined growth of ultrafine nanoparticles and restrains their aggregation, thus improving the stability of the embedded nanoparticles,[38,39] especially for the halide perovskites.[40–43] Inspired by these benefits, we encapsulated the lead-free double perovskite (CABB) in situ in the pores of the earth-abundant Fe-contained MOF (MIL-101(Fe)) to construct a series of CABB/MIL-101(Fe) composites. Of note, MIL-101(Fe) possesses a high selectivity for the photoreduction of CO_2 to HCOOH with the aid of a sacrificial agent,[44] while CABB exhibits a good ability to photooxidize CH_3OH to HCOOH in our preliminary experiments. The close proximity of CABB and MIL-101(Fe) facilitates effective interfacial charge separation, and thus CABB and MIL-101(Fe) can drive the CH_3OH oxidation and CO_2 reduction reactions to the same product HCOOH, respectively. CABB/MIL-101(Fe) composite can exhibit an impressive HCOOH yield of 1375 $\mu mol\, g^{-1}\, h^{-1}$ associated with a high selectivity of 97.8%, which is far superior to that of individual MIL-101(Fe) counterpart.

2. Results and Discussion

2.1. Morphology and Composition of CABB/MIL-101(Fe)

The CABB/MIL-101(Fe) composites were prepared via a one-pot synthesis strategy as illustrated in Scheme S1, Supporting Information, which is favorable for the uniform dispersion of ultrafine nanoparticles in the pores of MOF.[41] The synthesis details are summarized in the Experimental Section. Briefly, a certain amount of pre-prepared CABB nanocrystals was first added into the *N, N*- dimethylformamide solution of terephthalic acid and $FeCl_3{\cdot}6H_2O$, and then the mixed solution was hydrothermally treated at 110 °C for 24 h. After washing and sintering of the precipitate, the CABB/MIL-101(Fe) composites can be obtained. Depending on the amount of added as-prepared CABB (100, 200, and 300 mg), the corresponding composites were coded as $CABB^{100}$/MIL-101(Fe), $CABB^{200}$/MIL-101(Fe), and $CABB^{300}$/MIL-101(Fe), respectively. As a reference, individual MIL-101(Fe) was also prepared by adopting the same method, except for the addition of CABB nanocrystals and the sintering procedure.

The results of high-resolution scanning electron microscopy (HRSEM) measurements reveal that the as-prepared MIL-101(Fe) possesses a regular octahedral configuration (**Figure 1**a and S1a, Supporting Information) with an average size of 0.8 μm (Figure S1b, Supporting Information). The X-ray diffraction (XRD) pattern of MIL-101(Fe) demonstrates the generation of pure phase MIL-101 (Figure S2, Supporting Information). $CABB^{200}$/MIL-101(Fe) composite was selected as a typical sample to investigate the influence of encapsulating CABB on the morphology of MIL-101(Fe). As shown in Figure 1b and S1c, Supporting Information, the as-prepared $CABB^{200}$/MIL-101(Fe) composite also displays an octahedral architecture, and its dimensions (Figure S1d, Supporting Information) do not change noticeably compared to the parent MIL-101(Fe), indicating that the introduction of CABB quantum dots does not disrupt the framework structure

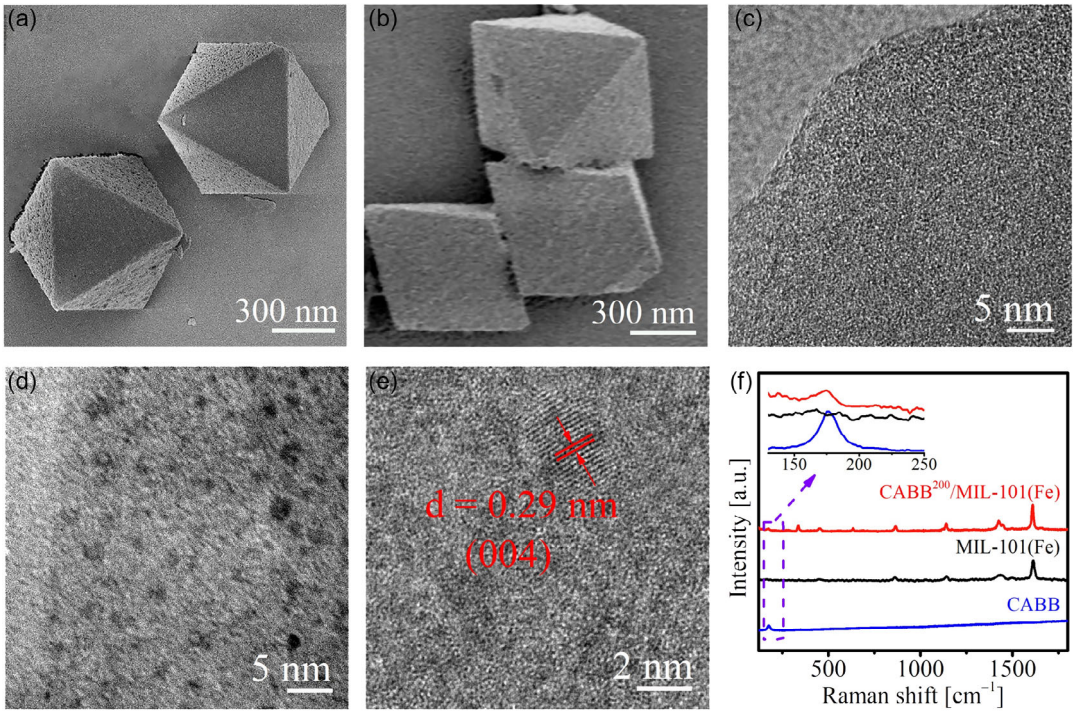

Figure 1. HRSEM images of a) MIL-101(Fe) and b) $CABB^{200}$/MIL-101(Fe). HRTEM images of c) MIL-101(Fe) and d) $CABB^{200}$/MIL-101(Fe). e) HRTEM image labeling the lattice spacing of $CABB^{200}$/MIL-101(Fe). f) Raman spectra of CABB, MIL-101(Fe) and $CABB^{200}$/MIL-101(Fe).

of MIL-101(Fe). In addition, neither the HRSEM (Figure 1b) nor the high-resolution transmission electron microscopy (HRTEM) images (Figure S3, Supporting Information) of $CABB^{200}$/MIL-101(Fe) show obvious large nanoparticles on its surface, suggesting that the CABB quantum dots should be encapsulated in the cavities of MIL-101(Fe), because CABB tends to form large nanoparticles if there is no spatial restraint.[45] Compared to the uniform HRTEM image of MIL-101(Fe) with local magnification (Figure 1c), evenly dispersed nanocrystals can be distinctly observed in the corresponding HRTEM image of $CABB^{200}$/MIL-101(Fe) (Figure 1d). The particle size analysis reveals that the quantum dots are approximately 2 nm in size (Figure S4, Supporting Information), slightly smaller than the two quasi-spherical cages in MIL-101(Fe) (29 and 34 Å).[46] Moreover, the lattice spacing of 0.29 nm can be clearly identified for the quantum dots (Figure 1e), which can be assigned to the (004) lattice plane of cubic phase CABB,[47] demonstrating the successful formation of CABB in the pores of MIL-101(Fe).

The characteristic diffraction peaks of individual MIL-101(Fe) can be clearly observed in the XRD patterns of $CABB^x$/MIL-101(Fe) composites (Figure S2, Supporting Information), and the Fourier transform infrared (FTIR) spectrum of composites (Figure S5, Supporting Information) is very similar to that of pristine MIL-101(Fe), proving once again that the encapsulation of ultrafine CABB in the pores of the MIL-101(Fe) does not destruct its framework structure. Nevertheless, the characteristic diffraction peaks corresponding to CABB cannot be found in the XRD patterns of the CABB/MIL-101(Fe) composites, which should be ascribed to the ultrafine size of CABB originated from spatial confinement of MIL-101(Fe) cages.[42] The successful incorporation of CABB in the MIL-101(Fe) can be further confirmed by Raman spectroscopy measurements. As shown in Figure 1f and S6, Supporting Information, apart from the characteristic peaks at 865, 1142, 1425, and 1612 cm^{-1} of MIL-101(Fe),[48] the Raman spectra of CABB/MIL-101(Fe) composites also show typical Raman signal for CABB (174.6 cm^{-1}).[49] Moreover, high-angle annular dark-field scanning TEM (HAADF-STEM) (**Figure 2**a) and energy-dispersive X-ray spectroscopy (EDS) mapping measurements (Figure 2b–h) disclosed that C, Fe, O, Cs, Ag, Bi, and Br elements are uniformly distributed in the MIL-101(Fe) framework, indicating that the CABB quantum dots are homogeneously dispersed in MIL-101(Fe). In addition, inductively coupled plasma mass spectrometry (ICP-MS) analysis (Figure S7 and Table S1, Supporting Information) revealed that the actual contents of CABB in $CABB^x$/MIL-101(Fe) composites increased with the amount of added CABB precursor. The mass percentages of CABB in $CABB^{100}$/MIL-101(Fe), $CABB^{200}$/MIL-101(Fe), and $CABB^{300}$/MIL-101(Fe) are calculated to be 3.4%, 7.9%, and 10.6%, respectively.

The successful deposition of CABB in the pores of MIL-101(Fe) can be further verified by recording the N_2 adsorption isotherms of MIL-101(Fe) and CABB/MIL-101(Fe) composites at 77 K and analyzing their porosities. As shown in Figure S8, Supporting Information, the total N_2 uptakes of all the CABB/MIL-101(Fe) composites are noticeably lower than that of MIL-101(Fe), and gradually decrease with the increasing amount of CABB. All the N_2 adsorption isotherms can be fitted well with BET model (Figure S9, Supporting Information), and the corresponding surface areas of MIL-101(Fe) and CABB/MIL-101(Fe) composites can be obtained accordingly, as summarized in Table S2, Supporting Information. The BET surface area of pristine MIL-101(Fe) is up to 2970 $m^2 g^{-1}$, indicating that MIL-101(Fe) is highly porous. The BET surface areas of $CABB^{100}$/MIL-101(Fe), $CABB^{200}$/MIL-101(Fe), and $CABB^{300}$/MIL-101(Fe) composites are significantly reduced to 1956, 944, and 745 $m^2 g^{-1}$,

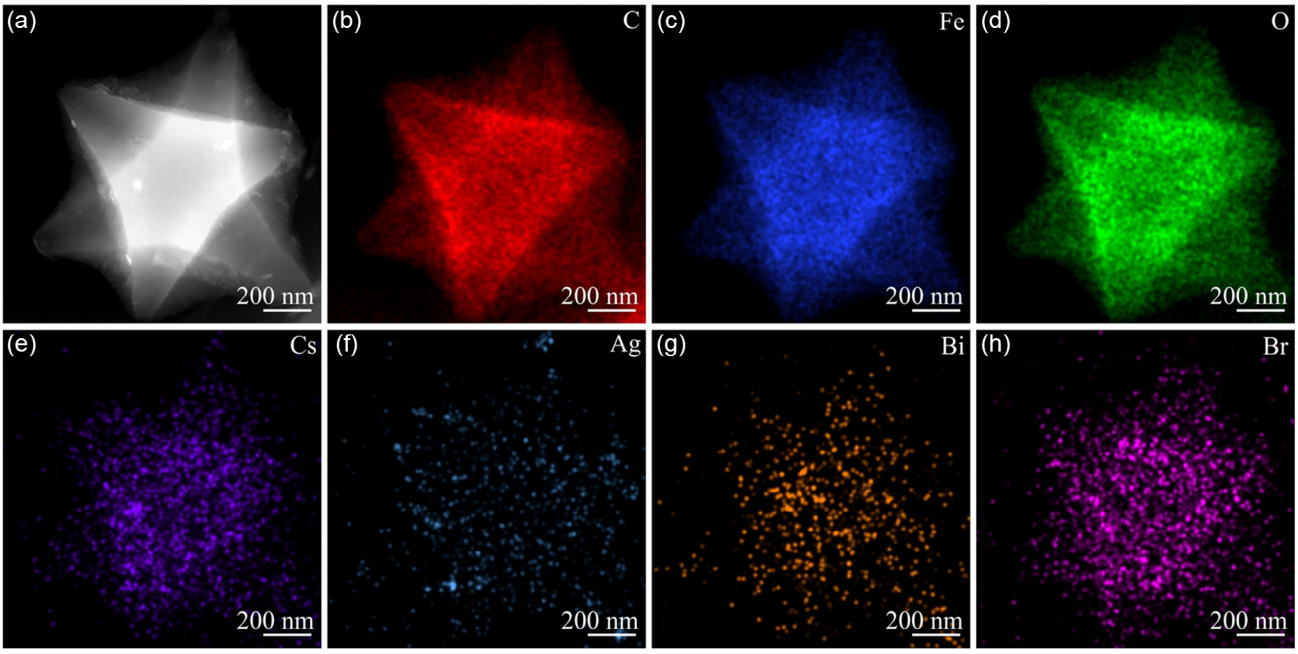

Figure 2. a) HAADF-STEM image and b–h) EDS elemental mapping images of $CABB^{200}$/MIL-101(Fe) composite: b) C, c) Fe, d) O, e) Cs, f) Ag, g) Bi, and h) Br.

respectively, which suggest that more and more pores of MIL-101(Fe) were occupied with the increase of CABB quantum dots. This speculation can be further confirmed by analyzing the pore size distribution of individual MIL-101(Fe) and CABB/MIL-101(Fe) composites, which can be derived by employing NLDFT model to fit the N_2 adsorption isotherms.[50] As depicted in Figure S10, Supporting Information, it can be clearly observed that the number of filled pores in the composites increases with the increase of CABB content by analyzing the vertical axis values of pore size distribution plots. Furthermore, the pore sizes of CABB/MIL-101(Fe) composites are smaller than that of pristine MIL-101(Fe) and decrease with the increasing amount of CABB quantum dots. The reduction in the surface area of CABB/MIL-101(Fe) relative to pristine MIL-101(Fe) also leads to a diminished ability for them to capture CO_2, which can be further confirmed by monitoring their CO_2 adsorption–desorption isotherms (Figure S11, Supporting Information).

2.2. Interaction and Charge Transfer at the Interface of CABB/MIL-101(Fe)

X-ray photoelectron spectroscopy (XPS) measurements were performed to investigate the interaction between MIL-101(Fe) and CABB in the CABB^{200}/MIL-101(Fe) composite. As shown in **Figure 3**a,b, the binding energies of Fe 2*p* and O 1*s* in CABB^{200}/MIL-101(Fe) are noticeably higher than those in MIL-101(Fe) by 0.20–0.35 eV. Meanwhile, all the peaks of Cs 3*d*, Ag 3*d*, Bi 4*f*, and Br 3*d* in CABB^{200}/MIL-101(Fe) (Figure 3c–f) are perceptibly shifted toward lower binding energy relative to those in CABB nanocrystal (Cs 3*d*: 0.10–0.15 eV, Ag 3*d*: ≈0.20 eV, Bi 4*f*: ≈0.45 eV, Br 3*d*: ≈ 0.25 eV). The apparent differences in elemental binding energy between CABB^{200}/MIL-101(Fe) and individual components imply a strong electronic coupling between MIL-101(Fe) and CABB, which should facilitate the interfacial transfer of photogenerated charges in the composite. Moreover, these enlargements and reductions in binding energy represent a decrease and an increase in the concentration of electrons around the nucleus, respectively, which means that partial free electrons in MIL-101(Fe) are transferred to CABB during the formation of CABB^{200}/MIL-101(Fe) composite. Therefore, the interface between MIL-101(Fe) and CABB in CABB^{200}/MIL-101(Fe) will generate a built-in electric field from MIL-101(Fe) toward CABB.

The thermodynamic properties of MIL-101(Fe) and CABB were further investigated by recording their ultraviolet−visible diffuse reflectance spectra (UV−vis DRS) and ultraviolet photoelectron spectra (UPS). As presented in Figure S12, Supporting Information, CABB exhibits significantly enhanced light absorption in the visible region relative to MIL-101(Fe), and thus the light-harvesting capacities of CABB/MIL-101(Fe) composites are appreciably stronger than that of MIL-101(Fe). According to the Tauc plots of MIL-101(Fe) and CABB (Figure S13, Supporting Information) transformed from corresponding UV−vis DRS spectra, the bandgaps of MIL-101(Fe) and CABB can be determined to be 2.80 and 2.07 eV, respectively, which are in good agreement with previous reports.[51,52] In addition, the valence band edge potentials (E_{VB}) of MIL-101(Fe) and CABB can be calculated in virtue of UPS measurements (**Figure 4**a), locating at 2.47 and 1.58 V versus the standard hydrogen electrode (SHE), respectively. This difference in E_{VB} between MIL-101(Fe) and CABB can be further confirmed by the result (0.88 V) derived from the XPS valence band spectra (Figure 4b). Therefore, MIL-101(Fe) possesses a more positive conduction band edge potential (E_{CB}) of −0.33 V in comparison with CABB (−0.49 V), which is well consistent with the measured flat-band potentials (MIL-101(Fe): −0.29 V; CABB: −0.44 V) derived from Mott−Schottky plots (Figure 4c,d). Apparently, coupling MIL-101(Fe) and CABB will form a Type II heterojunction as visualized in Figure 4e.

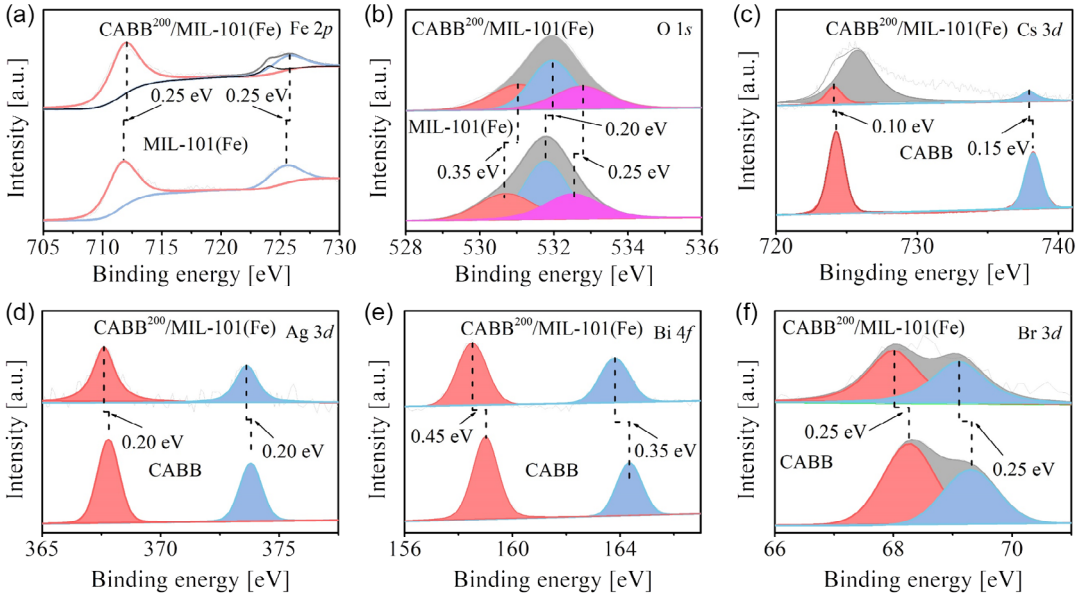

Figure 3. High-resolution XPS spectra of a) Fe 2*p* and b) O 1*s* in MIL-101(Fe) and CABB^{200}/MIL-101(Fe), c) Cs 3*d*, d) Ag 3*d*, e) Bi 4*f*, and f) Br 3*d* in CABB and CABB^{200}/MIL-101(Fe).

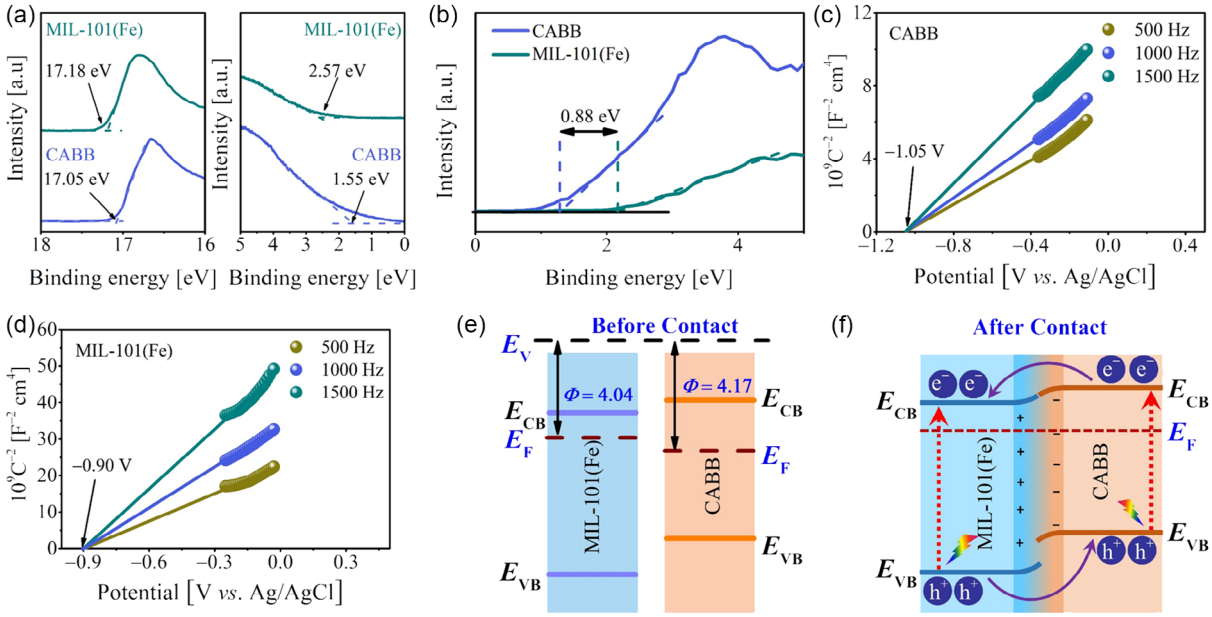

Figure 4. a) UPS spectra, b) XPS valence spectra, and c,d) Mott–Schottky plots of CABB and MIL-101(Fe). e) Energy band structures of CABB and MIL-101(Fe) before contact. f) Energy band structures and the most conceivable photogenerated carrier transfer pathway in CABB/MIL-101(Fe) composite. E_v, Φ, E_F, E_{CB}, and E_{VB} are on behalf of vacuum energy level, work function, Fermi energy level, conduction band, and valence band edges, respectively.

The migration origin of interfacial free electrons during the formation of CABB/MIL-101(Fe) composites can be disclosed by analyzing the difference in the Fermi energy levels (E_F) of MIL-101(Fe) and CABB. According to the UPS measurements (Figure 4a), the work function (Φ) of MIL-101(Fe) and CABB can be determined as 4.04 and 4.17 eV versus vacuum, respectively, and thus the respective E_F of MIL-101(Fe) and CABB are −4.04 and −4.17 eV as illustrated in Figure 4e. To achieve E_F equilibrium in the heterojunction system, the higher E_F of MIL-101(Fe) relative to CABB will result in the transfer of free electrons from MIL-101(Fe) to CABB when they are in close proximity, which is in line with the aforementioned results of XPS measurements. The transfer pathway of free electrons between MIL-101(Fe) and CABB can also be confirmed by electron paramagnetic resonance (EPR) measurements. As presented in Figure S14, Supporting Information, CABB^{200}/MIL-101(Fe) exhibits a stronger Fe^{3+} signal compared to MIL-101(Fe) in the dark, indicating the flow of free electrons from MIL-101(Fe) to CABB. The resultant built-in electric field as well as energy band bending facilitate the separation of photogenerated carriers in CABB^{200}/MIL-101(Fe) heterojunction following the typical double-charge transfer pathway (Figure 4f), which can be further demonstrated by the in situ irradiated XPS (ISI-XPS) measurements.[53] As presented in **Figure 5**a,b, light irradiation brings forth a distinct decrease in the binding energy for both Fe 2*p* (0.45 eV) and O 1*s* (0.20–0.40 eV) belonging to MIL-101(Fe). On the contrary, there are perceptible positive movements for all the binding energies of Cs 3*d* (0.10–0.15 eV), Ag 3*d* (0.40 eV), Bi 4*f* (0.40–0.45 eV), Br 3*d* (0.30–0.35 eV) associated with CABB upon illumination as depicted in Figure 5c–f. These results indicate that photogenerated electrons and holes accumulate in MIL-101(Fe) and CABB, respectively, which is in accordance with the double-charge transfer mechanism.

EPR measurements were further carried out to confirm the transfer orientation of photogenerated carriers in the interface of CABB/MIL-101(Fe) composites. As shown in Figure 5g, the EPR signal corresponding to Fe^{3+} of individual MIL-101(Fe) displays moderate quenching relative to the initial state after 5 min of light irradiation, and the degree of quenching intensifies as the illumination time is extended to 10 min. Under the same condition, it can be clearly observed that the Fe^{3+}-related signal in CABB^{200}/MIL-101(Fe) significantly diminishes following exposure to light for 5 min, and almost disappears after 10 min of light irradiation (Figure 5h), implying that effective electrons transfer from CABB to MIL-101(Fe) in CABB^{200}/MIL-101(Fe). These phenomena also proved that Fe is the main reduction reaction site for both MIL-101(Fe) and CABB^{200}/MIL-101(Fe). The efficient charge separation can be further demonstrated by the transient photocurrent (*I*–*t*) curve and electrochemical impedance spectrum (EIS) measurements under light irradiation. As presented in Figure S15, Supporting Information, CABB^{200}/MIL-101(Fe) exhibits notably larger photocurrent density, smaller charge transfer resistance, and longer lifetime of photogenerated electrons in comparison to MIL-101(Fe) and CABB.

2.3. Photocatalytic CO_2 Reduction and Methanol Oxidation Activity of CABB/MIL-101(Fe)

The photocatalytic CO_2 reduction activities of CABB/MIL-101(Fe) composites were evaluated in a mixture solvent of acetonitrile, CH_3OH, and water with saturated CO_2, and the experiment details are described in the experimental section. In addition, the performance of pristine MIL-101(Fe) was also

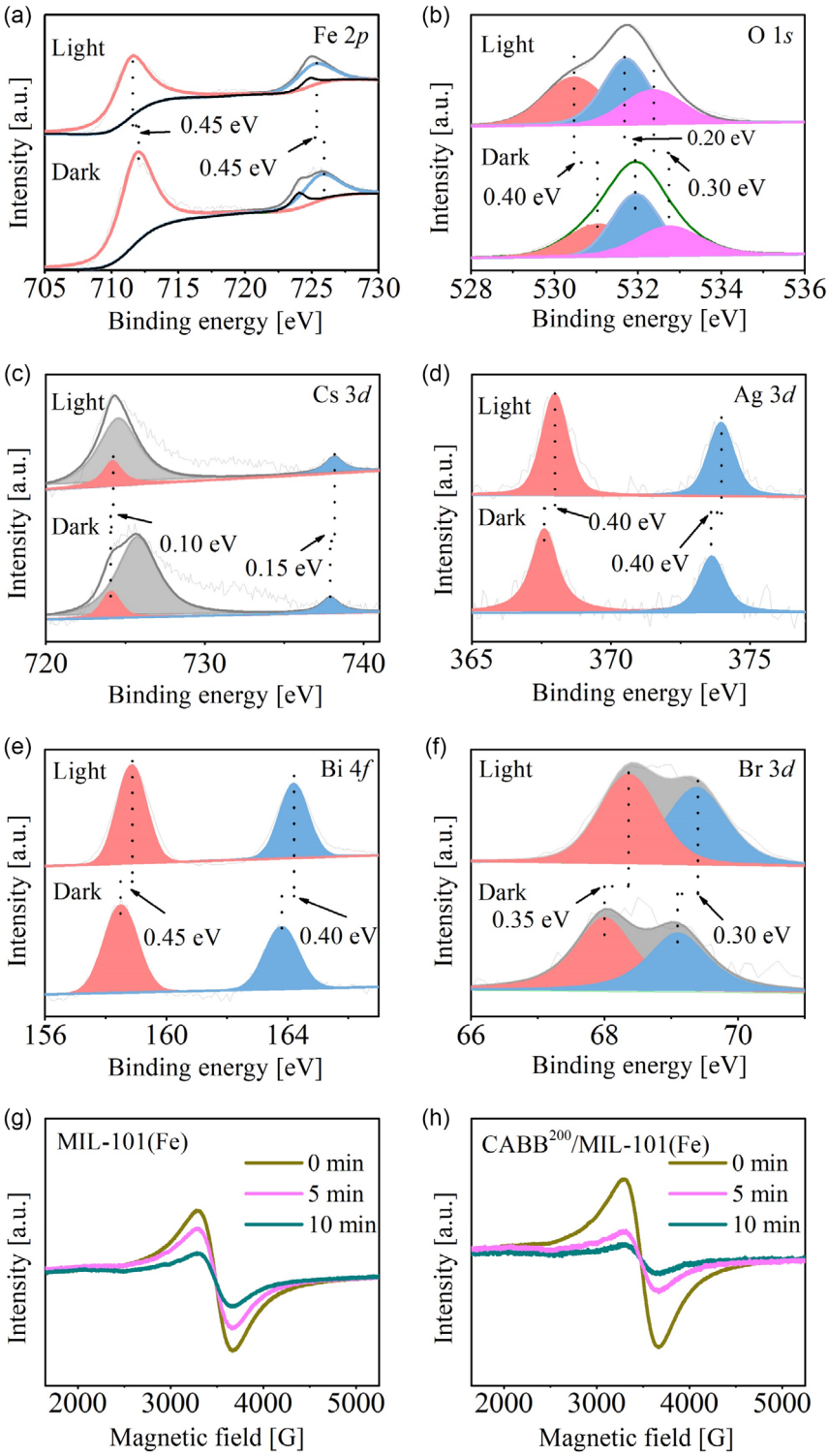

Figure 5. a–f) High-resolution XPS spectra of CABB^{200}/MIL-101(Fe) in the dark and under Xe lamp irradiation: a) Fe 2*p*, b) O 1s, c) Cs 3*d*, d) Ag 3*d*, e) Bi 4*f*, and f) Br 3*d*. EPR spectra of g) MIL-101(Fe) and h) CABB^{200}/MIL-101(Fe) before and after Xe lamp irradiation.

assessed under the same conditions as a reference. Gas chromatography measurements confirmed that no gas phase products can be detected for both MIL-101(Fe) and CABB/MIL-101(Fe) composites (Figure S16, Supporting Information). Ion chromatography (**Figure 6**a and S17, Supporting Information) measurements confirmed the main liquid product is HCOOH, where the

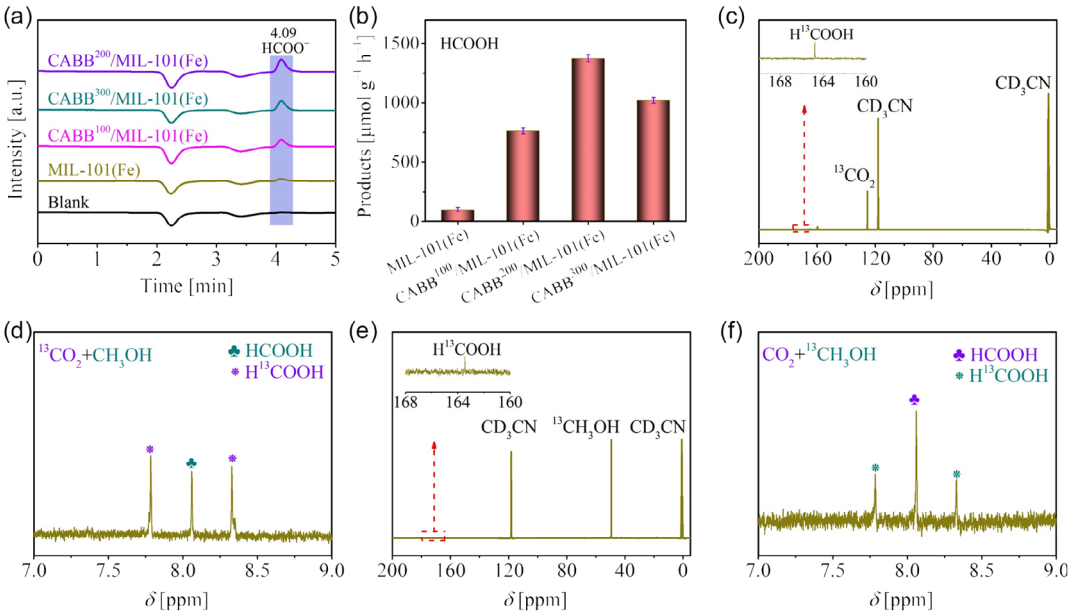

Figure 6. a) Ion chromatography curves of products with MIL-101(Fe) and CABB^{200}/MIL-101(Fe) as photocatalysts. b) The yields of HCOOH with MIL-101(Fe) and CABB^{x}/MIL-101(Fe) as photocatalysts. c) The ^{13}C NMR and d) ^{1}H NMR spectra of products in the reaction system containing $^{13}CO_2$ and CH_3OH. e) The ^{13}C NMR and f) ^{1}H NMR spectra of products in the reaction system containing CO_2 and $^{13}CH_3OH$.

corresponding characteristic peak at the retention time of 4.09 min can be detected. Further acetylacetone color chromogenic analyses (Figure S18, Supporting Information) revealed a trace amount of HCHO production. The yields of HCOOH and HCHO are compiled in Figure 6b and S19, Supporting Information. It is noted that the yield of HCOOH for pristine MIL-101(Fe) is only 98 μmol g^{-1} h^{-1}, which should be attributed to its rapid recombination of photogenerated carriers and weak response in the visible region. Under the same conditions, it is noted that the main reduction product for individual CABB is CO with a yield of 101 μmol g^{-1} h^{-1} (Table S3, Supporting Information), which is consistent with the previously reported result.[54]

In situ encapsulating CABB into the MIL-101(Fe) can bring forth a dramatically enhanced activity for photocatalytic CO_2 reduction coupled with CH_3OH oxidation with a high selectivity of HCOOH over 97% (Table S4, Supporting Information), owing to the improved light-harvesting and efficient separation of photogenerated carriers, which can overcompensate the disadvantageous influence of reduced CO_2 absorption. The performance of CABB/MIL-101(Fe) composites exhibit a common volcanic trend along with the increment of CABB content, and the highest yield of HCOOH can reach up to 1375 μmol g^{-1} h^{-1} (Figure 6b) with CABB^{200}/MIL-101(Fe) as photocatalyst, which is more than 14 times higher than that of MIL-101(Fe). Moreover, the corresponding selectivity of HCOOH is as high as 97.8%, indicating that CABB^{200}/MIL-101(Fe) photocatalyst can simultaneously achieve CO_2 reduction and CH_3OH oxidation to the uniform product of HCOOH. It is noted that there is a dramatic decrease in the photocatalytic performance in the absence of water in the reaction system because the activation of water is considered to be a prerequisite for the oxidation of methanol by forming surface-bonded OH,[55] which can promote the dehydrogenation process of methanol and provide the oxygen donor for the methanol oxidation to HCOOH.[56] Furthermore, SEM, XRD, and XPS measurements (Figure S20–S22, Supporting Information) revealed that the morphology and composition of CABB^{200}/MIL-101(Fe) can be well maintained after the photocatalytic reaction, demonstrating the good stability of the as-prepared CABB^{200}/MIL-101(Fe).

To identify the origin of the HCOOH product, isotope-labeling experiments were carried out with $^{13}CO_2$ and $^{13}CH_3OH$ as feedstocks. For the reaction system involving $^{13}CO_2$ and CH_3OH, the characteristic peak at 164.7 ppm assigned to H^{13}COOH can be observed in the ^{13}C NMR spectrum of the products (Figure 6c), demonstrating that CO_2 photoreduction is one of the carbon sources of HCOOH. In addition, two split peaks at 7.8 and 8.3 ppm can be clearly observed in the ^{1}H NMR spectrum of the products with $^{13}CO_2$ and CH_3OH as feedstocks (Figure 6d), which is ascribed to the coupling of the proton with the ^{13}C in H^{13}COOH.[57] Meanwhile, a typical singlet corresponding HCOOH ($\delta = 8.1$ ppm) can also be identified, indicating that part of the HCOOH should be originated from CH_3OH oxidation. Moreover, the integrated area ratio of peaks belonging to H^{13}COOH and HCOOH is 2.1:1, which is close to the inverse stoichiometric ratio between the number of charges required for CO_2 reduction (two electrons) and CH_3OH oxidation (four holes) to HCOOH. The slightly low yield of HCOOH from CH_3OH oxidation should be attributed to little CH_3OH oxidized to HCHO. In the ^{13}C NMR spectrum of the products with CO_2 and $^{13}CH_3OH$ as feedstocks (Figure 6e), the characteristic peak assigned to H^{13}COOH can also be clearly identified, further confirming that partial HCOOH indeed originated from CH_3OH oxidation. This speculation can be proven again by analyzing

the corresponding ^{1}H NMR spectrum (Figure 6f), where both the doublet associated with $H^{13}COOH$ and the singlet assigned to HCOOH can also be observed. In addition, the integrated area ratio of peaks originated from CO_2 reduction and CH_3OH oxidation can be calculated to be 2.08:1, which is consistent with the measured value in the system containing $^{13}CO_2$ and CH_3OH. In addition, we also carried out a series of control experiments. When using Ar to replace CO_2, there is trace HCOOH. Without light irradiation or photocatalyst, no HCOOH can be detected (Table S5, Supporting Information), further conforming that the HCOOH product originates from CO_2 photoreduction and methanol photooxidation.

2.4. Photocatalytic Mechanism of CABB/MIL-101(Fe)

To unravel the reaction pathways of CO_2 reduction and CH_3OH oxidation, in situ FTIR spectroscopy measurements were carried out to gain the reaction intermediates with $CABB^{200}$/MIL-101(Fe) as photocatalyst at different reaction times. As shown in **Figure 7**a, when CO_2 was continuously bubbling through CH_3OH aqueous solution, the characteristic signals of intermediates could not be detected at 0 min of light. While the typical peaks arising at the range of 2800–3000 cm^{-1} can be clearly observed after the light illumination, which can be attributed to the stretching and bending vibration peaks of C—H in $*OCH_3$.[58] Upon light irradiation, the signals of peaks at 2981, 2945, 2921, 2864, 2842, and 2831 cm^{-1} were enhanced significantly with the extension of reaction time, indicating that CH_3OH oxidation reaction is driven by the photogenerated holes in $CABB^{200}$/MIL-101(Fe). Furthermore, two characteristic peaks of C—O in $*OCH_3$ intermediate at 1060 and 1112 cm^{-1} also showed an increase in peak intensity with prolonged reaction time (Figure 7b). The peak at 1025 cm^{-1} can be assigned to the CH_3OH adsorbed on the surface of the catalyst. In addition, the bands at 1393 and 1550 cm^{-1} can be attributed to the O—C—O asymmetric stretch in the intermediate of *OCHO, which comes from the oxidation of CH_3OH. These phenomena imply that CH_3OH oxidation begins with the breakage of O—H bond, followed by a multistep dehydrogenation process of the methyl group.[59] The peak at 1612 cm^{-1} originated from the adsorption of water. The typical peaks of *OCHO that come from CO_2 photoreduction arising at 1452 and 1479 cm^{-1} can be clearly observed after the light illumination, suggesting that CO_2 is coordinated to the unsaturated Fe sites on the surface of $CABB^{200}$/MIL-101(Fe) via two oxygen atoms.[60] The intensity of the peaks at 1452 and 1479 cm^{-1} rises as extending reaction time, indicating that the CO_2 reduction reaction is driven by photo-generated electrons.

Based on the above results, the reaction pathways of photocatalytic CO_2 reduction coupled with CH_3OH oxidation over CABB/MIL-101(Fe) can be proposed, as illustrated in Figure 7c. First, photoexcitation produces electron–hole pairs in both MIL-101(Fe) and CABB. Subsequently, the photogenerated carriers achieve effective charge separation at the close contact interface between MIL-101(Fe) and CABB via double-charge transfer mode, leading to the accumulation of photogenerated electrons and holes in MIL-101(Fe) and CABB, respectively.

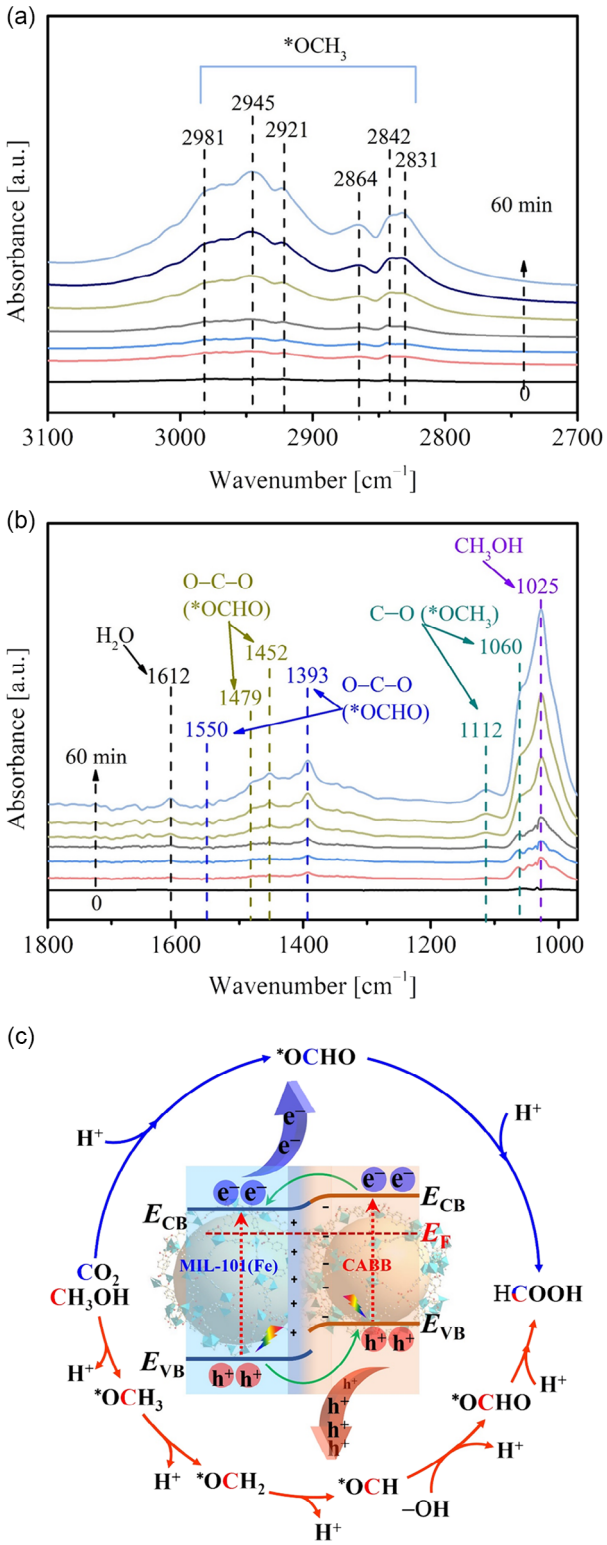

Figure 7. Operando FTIR spectra of intermediates were recorded at different reaction times with the $CABB^{200}$/MIL-101(Fe) as the photocatalyst. a) 970–1800 cm^{-1} and b) 2700–3100 cm^{-1}. c) Schematic illustration for the proposed reaction pathways of CO_2 reduction and CH_3OH oxidation on bifunctional photocatalysts of CABB/MIL-101(Fe).

Thereafter, the photogenerated electrons in the conduction band of MIL-101(Fe) trigger reduction reaction of bidentate coordinated CO_2 to form *OCHO intermediate on the Fe site via a proton-coupled electron transfer pathway, followed by further proton-coupled electron transfer reaction to generate HCOOH. Meanwhile, the photogenerated holes in the valence band of CABB activate the O—H bond of CH_3OH to generate *OCH_3 intermediate, which undergoes a multistep dehydrogenation process to produce *OCH. Then, *OCH intermediate captures an O atom from OH group to form *OCHO intermediate, followed by accepting a proton and desorbing to give the product HCOOH.

3. Conclusion

In summary, a series of bifunctional photocatalysts of CABB/MIL-101(Fe) has been successfully prepared based on a facial one-pot synthesis strategy. The as-prepared composites possess strong electron coupling and suitable energy offset between MIL-101(Fe) and CABB, which bring forth an efficient charge separation via typical double-charge transfer mode as demonstrated by XPS, UPS, photoelectrochemical, and EPR measurements. The resultant efficient spatial separation of photogenerated carriers enables the composites to achieve highly selective photosynthesis of HCOOH by unifying the products of CO_2 reduction and CH_3OH oxidation as confirmed by isotope-labeling experiments and NMR analyses. An impressive yield of 1375 $\mu mol\, g^{-1}\, h^{-1}$ with a high selectivity of 97.8% for HCOOH generation can be achieved over $CABB^{200}$/MIL-101(Fe) photocatalyst. The strategy presented here for unifying redox products could be extended to other organic reactions integrated with CO_2 reduction by the elaborate design of photocatalysts, opening a new window for the effective resourceful utilization of CO_2.

4. Experimental Section

Synthesis of MIL-101(Fe) Octahedron: 206 mg of terephthalic acid (H_2BDC) and 675 mg of $FeCl_3{\cdot}6H_2O$ were dissolved in 15 mL *N, N*-dimethylformamide (DMF). The mixture was heated at 110 °C for 24 h in a high-pressure autoclave (25 mL), and then cooled to room temperature naturally.[44] Afterward, the mixture was centrifuged and further purified with hot DMF and ethanol to obtain the MIL-101(Fe) octahedron.

Synthesis of $Cs_2AgBiBr_6$ (CABB) Nanocrystals: CABB was synthesized by modifying some previously reported methods.[45] Briefly, AgBr was prepared by the reaction of HBr and $AgNO_3$ at room temperature. Then, AgBr (89 mg), CsBr (218 mg), and $BiBr_3$ (225 mg) were mixed with 10 mL of HBr solution. The mixture was heated to 110 °C with stirring under closed conditions for 2 h, and then cooled to room temperature, followed by keeping unperturbed for 1 h to generate orange precipitation. Subsequently, the as-prepared precipitation was washed with ethanol for three times, and then dissolved into 4 mL of dimethyl sulfoxide (DMSO) solvent. Finally, CABB nanocrystals can be obtained by adding 30 mL of isopropanol into the DMSO solution, followed by washing with ethanol after centrifugation.

Synthesis of $CABB^x$/MIL-101(Fe): Typically, 206 mg of H_2BDC and 675 mg of $FeCl_3{\cdot}6H_2O$ were dissolved in 15 mL of DMF. Thereafter, CABB (100, 200, or 300 mg) was added into the solution under stirring. The mixture was transferred into a 25 mL Teflon-lined autoclave after CABB was completely dissolved. The autoclave was treated at 110 °C for 24 h, and then cooled to room temperature naturally. The obtained samples were washed two times with DMF and soaked in 6 mL of ethanol for 12 h, then centrifuged and dried in a vacuum at 60 °C. Finally, the sample was calcinated in a tube furnace at 150 °C for 2 h to completely remove the DMF solvent and obtain the $CABB^x$/MIL-101(Fe) composites.

Photocatalytic Experiments: The photocatalytic reaction of CO_2 reduction concurrent with CH_3OH oxidation was performed in a 25 mL sealed quartz bottle. Typically, photocatalyst (3 mg), acetonitrile (4 mL), CH_3OH (2 mL), and water (100 μL) were added into the reaction system. Before the photocatalytic reaction, the reaction apparatus was degassed and refilled with CO_2 for 40 min to remove air. A 300 W Xe lamp (CEL-HXF300, CEAULICHT) was used to simulate the solar light illumination. The products were detected after 4 h of photocatalytic reaction.

Product Analysis: The gas products were detected quantitatively using GC-2014 gas chromatograph instrument (Agilent) equipped with a thermal conductivity detector (TCD) and a flame ionization detector (FID). The production of HCOOH was determined using an ion chromatograph (Metrohm ECO) equipped with an anion analysis column (Metrosep A Supp 5-150/4.0). The corresponding standard curve was established with the concentration of sodium formate solution. The production of HCHO was analyzed by traditional colorimetric approach.[58] Typically, ammonium acetate (12.5 g), acetic acid (0.5 mL), and pentane-2,4-dione (0.1 mL) were dissolved in 50 mL water to form color developing reagent solution. Then 1 mL of the reaction liquid was mixed with 1 mL reagent solution. The mixed solution was placed in a water bath (60 °C) for 20 min, followed by measuring its UV—vis absorption spectrum to quantify the concentration of HCHO according to a standard curve, which was established with 37 wt% formaldehyde aqueous solution.

Supporting Information

Supporting Information is available from the Wiley Online Library or from the author.

Acknowledgements

Z.-L.L. and M.-R.Z. contributed equally to this work. This work was financially supported by the National Key R&D Program of China (grant nos. 2022YFA1502902 and 2017YFA0700104), NSFC (grant nos. 21931007 and U21A20286), Natural Science Foundation of Tianjin City (grant no. 17JCJQJC43800), the 111 Project of China, and Tianjin Research Innovation Project for Postgraduate Students (grant no. 2022BKY153).

Conflict of Interest

The authors declare no conflict of interest.

Data Availability Statement

The data that support the findings of this study are available from the corresponding author upon reasonable request.

Keywords

CO_2 reduction, lead-free double perovskites, metal—organic frameworks, methanol oxidation, photocatalysis

Received: April 24, 2023
Revised: May 7, 2023
Published online:

[1] T. A. Jacobson, J. S. Kler, M. T. Hernke, R. K. Braun, K. C. Meyer, W. E. Funk, *Nat. Sustainable* **2019**, *2*, 691.
[2] S. J. Davis, N. S. Lewis, M. Shaner, S. Aggarwal, D. Arent, I. L. Azevedo, S. M. Benson, T. Bradley, J. Brouwer, Y.-M. Chiang,

C. T. M. Clack, A. Cohen, S. Doig, J. Edmonds, P. Fennell, C. B. Field, B. Hannegan, B.-M. Hodge, M. I. Hoffert, E. Ingersoll, P. Jaramillo, K. S. Lackner, K. J. Mach, M. Mastrandrea, J. Ogden, P. F. Peterson, D. L. Sanchez, D. Sperling, J. Stagner, J. E. Trancik, et al., *Science* **2018**, *360*, aas9793.
[3] S. Bushuyev, P. De Luna, C. T. Dinh, L. Tao, G. Saur, J. van de Lagemaat, S. O. Kelley, E. H. Sargent, *Joule* **2018**, *2*, 825.
[4] T. Inoue, A. Fujishima, S. Konishi, K. Honda, *Nature* **1979**, *277*, 637.
[5] S. Yoshino, T. Takayama, Y. Yamaguchi, A. Iwase, A. Kudo, *Acc. Chem. Res.* **2022**, *55*, 966.
[6] H. Huang, R. Shi, Z. Li, J. Zhao, C. Su, T. Zhang, *Angew. Chem. Int. Ed.* **2022**, *61*, e202200802.
[7] Q. Chen, X. Lan, Y. Ma, P. Lu, Z. Yuan, J. Shi, *Sol. RRL* **2021**, *5*, 2100186.
[8] X. Sun, L. Sun, G. Li, Y. Tuo, C. Ye, J. Yang, J. Low, X. Yu, J. H. Bitter, Y. Lei, D. Wang, Y. Li, *Angew. Chem. Int. Ed.* **2022**, *61*, e202207677.
[9] X. Lin, S. Xia, L. Zhang, Y. Zhang, S. Sun, Y. Chen, S. Chen, B. Ding, J. Yu, J. Yan, *Adv. Mater.* **2022**, *34*, 2200756.
[10] Z.-K. Xin, Y.-J. Gao, Y. Gao, H.-W. Song, J. Zhao, F. Fan, A.-D. Xia, X.-B. Li, C.-H. Tung, L.-Z. Wu, *Adv. Mater.* **2022**, *34*, 2106662.
[11] K. Su, S.-X. Yuan, L.-Y. Wu, Z.-L. Liu, M. Zhang, T.-B. Lu, *Small* **2023**, 2301192, https://doi.org/10.1002/smll.202301192.
[12] L. Chen, X. Yue, L. Wang, D. Zhang, P. Zhang, J. Fan, Q. Xiang, *Adv. Mater.* **2021**, *33*, 2105135.
[13] Q. Wang, J. Warnan, S. Rodríguez-Jiménez, J. J. Leung, S. Kalathil, V. Andrei, K. Domen, E. Reisner, *Nat. Energy* **2020**, *5*, 703.
[14] Y.-X. Feng, G.-X. Dong, K. Su, Z.-L. Liu, W. Zhang, M. Zhang, T.-B. Lu, *J. Energy Chem.* **2022**, *69*, 348.
[15] Y. Zhang, X. Zhi, J. R. Harmer, H. Xu, K. Davey, J. Ran, S.-Z. Qiao, *Angew. Chem. Int. Ed.* **2022**, *61*, e202212355.
[16] Y. Fang, Y. Hou, X. Fu, X. Wang, *Chem. Rev.* **2022**, *122*, 4204.
[17] S. Ye, C. Ding, M. Liu, A. Wang, Q. Huang, C. Li, *Adv. Mater.* **2019**, *31*, 1902069.
[18] P. Du, R. Qi, Y. Zhang, Q. Gu, X. Xu, Y. Tan, X. Liu, A. Wang, B. Zhu, B. Yang, T. Zhang, *Chem* **2022**, *8*, 3252.
[19] P. Verma, F. A. Rahimi, D. Samanta, A. Kundu, J. Dasgupta, T. K. Maji, *Angew. Chem. Int. Ed.* **2022**, *61*, e202116094.
[20] J.-C. Wang, N. Li, A. M. Idris, J. Wang, X. Du, Z. Pan, Z. Li, *Sol. RRL* **2021**, *5*, 2100154.
[21] W. Wu, C. Dai, M. Wu, Y. Chen, C. Zeng, F. Li, *Sol. RRL* **2023**, *7*, 2200907.
[22] Y. Wang, R. Godin, J. R. Durrant, J. Tang, *Angew. Chem. Int. Ed.* **2021**, *60*, 20811.
[23] W. Wang, C. Deng, S. Xie, Y. Li, W. Zhang, H. Sheng, C. Chen, J. Zhao, *J. Am. Chem. Soc.* **2021**, *143*, 2984.
[24] K. Kamada, J. Jung, T. Wakabayashi, K. Sekizawa, S. Sato, T. Morikawa, S. Fukuzumi, S. Saito, *J. Am. Chem. Soc.* **2020**, *142*, 10261.
[25] H. Liu, H.-L. Jiang, *Chem* **2019**, *5*, 2508.
[26] E. Lam, E. Reisner, *Angew. Chem. Int. Ed.* **2021**, *60*, 23306.
[27] H. Yu, E. Haviv, R. Neumann, *Angew. Chem. Int. Ed.* **2020**, *59*, 6219.
[28] R. Zhang, H. Wang, S. Tang, C. Liu, F. Dong, H. Yue, B. Liang, *ACS Catal.* **2018**, *8*, 9280.
[29] Q. Guo, F. Liang, X.-B. Li, Y.-J. Gao, M.-Y. Huang, Y. Wang, S.-G. Xia, X.-Y. Gao, Q.-C. Gan, Z.-S. Lin, C.-H. Tung, L.-Z. Wu, *Chem* **2019**, *5*, 2605.
[30] G.-X. Dong, W. Zhang, Y.-F. Mu, K. Su, M. Zhang, T.-B. Lu, *Chem. Commun.* **2020**, *56*, 4664.
[31] F. Wang, T. Hou, X. Zhao, W. Yao, R. Fang, K. Shen, Y. Li, *Adv. Mater.* **2021**, *33*, 2102690.
[32] C. Han, Y.-H. Li, J.-Y. Li, M.-Y. Qi, Z.-R. Tang, Y.-J. Xu, *Angew. Chem. Int. Ed.* **2021**, *60*, 7962.
[33] X. Gong, S. Yu, M. Guan, X. Zhu, C. Xue, *J. Mater. Chem. A* **2019**, *7*, 7373.
[34] J. Lodh, A. Mallick, S. Roy, *J. Mater. Chem. A* **2018**, *6*, 20844.
[35] L. Yuan, M.-Y. Qi, Z.-R. Tang, Y.-J. Xu, *Angew. Chem. Int. Ed.* **2021**, *60*, 21150.
[36] Q. Liu, J. Lin, H. Cheng, L. Wei, F. Wang, *Angew. Chem. Int. Ed.* **2023**, *62*, e202218720.
[37] X. Wang, X. Yang, C. Chen, H. Li, Y. Huang, R. Cao, *Acta Chim. Sin.* **2022**, *80*, 22.
[38] J. Cao, Z. Yang, W. Xiong, Y. Zhou, Y. Wu, M. Jia, C. Zhou, Z. Xu, *Coordin. Chem. Rev.* **2021**, *439*, 213924.
[39] Z. Jiang, X. Xu, Y. Ma, H. S. Cho, D. Ding, C. Wang, J. Wu, P. Oleynikov, M. Jia, J. Cheng, Y. Zhou, O. Terasaki, T. Peng, L. Zan, H. Deng, *Nature* **2020**, *586*, 549.
[40] C. Zhang, W. Li, L. Li, *Angew. Chem. Int. Ed.* **2021**, *60*, 7488.
[41] J. Hou, P. Chen, A. Shukla, A. Krajnc, T. Wang, X. Li, R. Doasa, L. H. G. Tizei, B. Chan, D. N. Johnstone, R. Lin, T. U. Schülli, I. Martens, D. Appadoo, M. S. Ari, Z. Wang, T. Wei, S.-C. Lo, M. Lu, S. Li, E. B. Namdas, G. Mali, A. K. Cheetham, S. M. Collins, V. Chen, L. Wang, T. D. Bennett, *Science* **2021**, *374*, 621.
[42] G.-Y. Qiao, D. Guan, S. Yuan, H. Rao, X. Chen, J.-A. Wang, J.-S. Qin, J.-J. Xu, J. Yu, *J. Am. Chem. Soc.* **2021**, *143*, 14253.
[43] L.-Y. Wu, Y.-F. Mu, X.-X. Guo, W. Zhang, Z.-M. Zhang, M. Zhang, T.-B. Lu, *Angew. Chem. Int. Ed.* **2019**, *58*, 9491.
[44] D. Wang, R. Huang, W. Liu, D. Sun, Z. Li, *ACS Catal.* **2014**, *4*, 4254.
[45] Z. Zhang, Y. Liang, H. Huang, X. Liu, Q. Li, L. Chen, D. Xu, *Angew. Chem. Int. Ed.* **2019**, *58*, 7263.
[46] M. Y. Zorainy, M. G. Alalm, S. Kaliaguine, D. C. Boffito, *J. Mater. Chem. A* **2021**, *9*, 22159.
[47] T. Wang, D. Yue, X. Li, Y. Zhao, *Appl. Catal. B Environ.* **2020**, *268*, 118399.
[48] Y. Gong, Y. Ding, Q. Tang, F. Lian, C. Bai, R. Xie, H. Xie, X. Zhao, *Chin. Chem. Lett.* **2023**, 108475, https://doi.org/10.1016/j.cclet.2023.108475.
[49] S. Yoon, B. Fett, A. Frebel, S. Kroisl, B. Herbig, M. Widenmeyer, B. Balke, G. Sextl, K. Mandel, A. Weidenkaff, *Energy Technol.* **2022**, *10*, 2200197.
[50] G. Kupgan, T. P. Liyana-Arachchi, C. M. Colina, *Langmuir* **2017**, *33*, 11138.
[51] Y. Xie, C. Liu, D. Li, Y. Liu, *Appl. Surf. Sci.* **2022**, *592*, 153312.
[52] A. H. Slavney, T. Hu, A. M. Lindenberg, H. I. Karunadasa, *J. Am. Chem. Soc.* **2016**, *138*, 2138.
[53] J. Low, B. Dai, T. Tong, C. Jiang, J. Yu, *Adv. Mater.* **2019**, *31*, 1802981.
[54] Y. Wang, H. Huang, Z. Zhang, C. Wang, Y. Yang, Q. Li, D. Xu, *Appl. Catal. B Environ.* **2021**, *282*, 119570.
[55] M. J. C. van der Niet, A. den Dunnen, L. B. F. Juurlink, M. T. M. Koper, *Angew. Chem. Int. Ed.* **2010**, *49*, 6572.
[56] M. T. M. Koper, S. C. S. Lai, E. Herrero, *Fuel Cell Catalysis: A Surface Science Approach* (Ed: M. T. M. Koper), Wiley, Hoboken **2009**, p. 159.
[57] K. Sekizawa, K. Maeda, K. Domen, K. Koike, O. Ishitani, *J. Am. Chem. Soc.* **2013**, *135*, 4596.
[58] L. J. Burcham, L. E. Briand, I. E. Wachs, *Langmuir* **2001**, *17*, 6164.
[59] W. Shan, R. Liu, H. Zhao, Z. He, Y. Lai, S. Li, G. He, J. Liu, *ACS Nano* **2020**, *14*, 11363.
[60] J. Chen, S. Stepanovic, A. Draksharapu, M. Gruden, W. R. Browne, *Angew. Chem. Int. Ed.* **2018**, *57*, 3207.